# Modeling the Hydrophobicity of Nanoparticles and Their Interaction with Lipids and Proteins

Ali Ramazani,[†] Taraknath Mandal,[†] and Ronald G. Larson*

Department of Chemical Engineering, University of Michigan, 2300 Hayward Street, Ann Arbor, Michigan, United States

S *Supporting Information*

ABSTRACT: We present a method of modeling nanoparticle (NP) hydrophobicity using coarse-grained molecular dynamics (CG MD) simulations, and apply this to the interaction of lipids with nanoparticles. To model at a coarse-grained level the wettability or hydrophobicity of a given material, we choose the MARTINI coarse-grained force field, and determine through simulation the contact angles of MARTINI water droplets residing on flat regular surfaces composed of various MARTINI bead types (C1, C2, etc.). Each surface is composed of a single bead type in each of three crystallographic symmetries (FCC, BCC, and HCP). While this method lumps together several atoms (for example, one cerium and two oxygens of CeO_2) into a single CG bead, we can still capture the overall hydrophobicity of the actual material by choosing the MARTINI bead type that gives the best fit of the contact angle to that of the actual material, as determined by either experimental or all-atom simulations. For different MARTINI bead types, the macroscopic contact angle is obtained by extrapolating the microscopic contact angles of droplets of eight different sizes (containing N_w = 3224−22978 water molecules) to infinite droplet size. For each droplet, the contact angle was computed from a best fit of a circular curve to the droplet interface extrapolated to the first layer of the surface. We then examine how small nanoparticles of differing wettability interact with MARTINI dipalmitoylphosphotidylcholine (DPPC) lipids and SP-C peptides (a component of lung surfactant). The DPPC shows a transition from tails coating the nanoparticle to a hemimicelle coating the water-wet NP, as the contact angle of a water droplet on the surface is lowered below ∼60°. The results are relevant to developing a taxonomy describing the potential nanotoxicity of nanoparticle interactions with components in the lung.
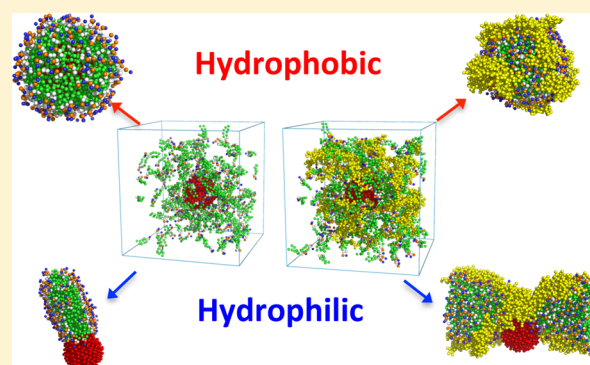
■ INTRODUCTION

Inorganic nanoparticles (NPs) play an important role in modern nanotechnology because of their applications in electronics,[1−4] optics,[5−9] and medicine[10−14] to name but a few. In particular, their potential applications in biomedical science, including bioimaging,[15−17] biosensing,[18−20] and drug delivery,[21−23] have drawn significant research interest. Recently, both the atomistic[24,25] and coarse-grained[26,27] molecular simulations have been performed extensively to investigate the role of morphology[26] (size and shape) and surface chemistry[28] of an NP in its interaction with membrane and lipids and proteins. Ramalho et al.,[27] for example, used coarse-grained simulations to investigate the effect of an NP on the structure and phase transformations of DPPC bilayers. Nangia et al.[29] studied the role of the shape of a NP on its translocation through cell membrane. Hu et al.[30] employed coarse-grained simulations combined with experiments to show how the physiochemical properties of NPs regulate translocation across the pulmonary surfactant monolayer. Simonelli et al.,[31] using computer simulations, described how monolayer-protected anionic NPs translocate into cell membranes step by step. Thus, simulation studies can predict the efficiency of a given

NP as a diagnostic and therapeutic agent and also help in rational designing of a better NP agent.

However, the complexity of structures of even model biosystems limits fully atomistic simulations to relatively short time and length scales. Hence, most of the above-mentioned simulation studies employed a coarse-grained model, often the MARTINI[32] coarse-grained force field, to reduce the numbers of degrees of freedom and to access longer time scales. In the MARTINI model, coarse-grained beads are categorized into polar (P), intermediate polar (N), and apolar (C), among other bead types, depending on their interaction strengths with the water beads. The polarity of a material determines its wettability, which is an important parameter for designing an efficient drug carrier. Apart from the biomedical applications, the MARTINI force field also has been used widely to model surfactants,[32,33] polymers,[34,35] biopolymers,[36,37] and inorganic materials.[38,39] Therefore, it is important to establish the wettability of a material made of the individual MARTINI beads. One important application of such a coarse-grained
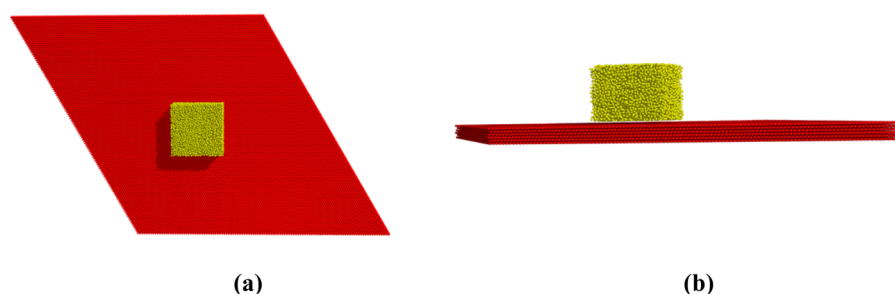
Figure 1. (a) Top and (b) side views of the initial water box (N_w = 9694) on an FCC (111) surface.
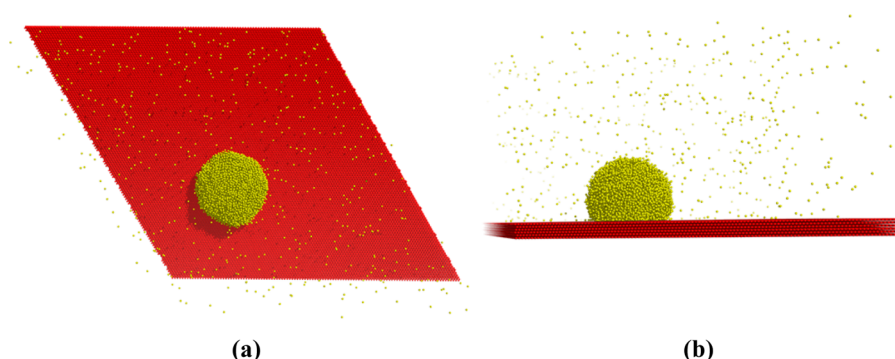

Figure 2. (a) Top and (b) side views of a water droplet (N_w = 9694) spread on a (111) FCC surface after a 120 ns MD simulation.

model is in the area of nanotoxicology, where nanoparticles ingested through the lung might make their way into organs of the body, possibly after acquiring a "corona" of lipids and proteins in the lung.[40] The hydrophobicity of the nanoparticle is expected to play an important role in determining what, if any, corona might form on such nanoparticles as a result of passage through the lung or other tissues. More generally, coarse-grained force fields such as MARTINI are widely used, and problems with interfaces, including both solid and liquid interfaces, are among the most important applications.[41−43] Thus, correlating MARTINI bead type with the wettability of a surface made of beads of that type constitutes a basic characterization that can guide selection of MARTINI bead types for applications to problems with interfaces more generally.

In this work, we use molecular dynamics (MD) simulations to model the wettability of materials at the coarse-grained level. We employ the MARTINI force field to model the material and then compute the contact angle of water on top of a flat surface. We note that the water forms a wide range of contact angles (120 to 20°) on flat surfaces made of different standard MARTINI beads (C1, C2, etc.). These, plus some new bead types that we specifically introduce to expand the number of contact angles available, allows us to systematically investigate the role of hydrophobicity of a given material on its interaction with various biomolecules such as lipids and proteins. We then explore the interaction of a small NP with DPPC lipids as a function of its wettability. Our results predict a transition from tails coating the nanoparticle to hemimicelle coating to water-wet NPs when the contact angle of the material is lower than 58°. We also investigate the role of SP-C peptides, a component of pulmonary surfactant, on the lipid−NP system. In the following, we first describe the methodology used in the simulation, then discuss the results, and finally provide a summary of the main results.

■ METHODOLOGY

To measure the microscopic contact angle of a water droplet, a cube of water is placed on top of a crystalline surface (approximately 60 nm × 60 nm), as shown in Figure 1. We consider eight different droplet sizes containing between 3224 and 22978 water beads. The macroscopic contact angle of a given bead type is obtained by extrapolating the microscopic contact angles of these droplets to infinite droplet size. Substrates of three different crystal symmetries (FCC, BCC, and HCP) are used to investigate how this affects the contact angle of water. The box lengths along the X and Y directions are taken to be the same as the dimension of the slab, and the box length along the perpendicular direction of the surface is set to be 25 nm. The simulation box is large enough to avoid interaction of the water droplet with its periodic images. Bad contacts between the water beads and the crystalline surface in the initial system are removed by steepest descent energy minimization. The system is then gradually heated up to 298 K temperature and equilibrated for 60 ns at constant volume and temperature. The equilibration step is followed by another 60 ns production run during which data are collected for analysis. A time step of 30 fs is chosen for both the equilibration and production runs. The temperature of the system is controlled by a V-rescale thermostat.[44] A cutoff distance of 1.2 nm is used for van der Waals interaction. All simulations are performed by using the GROMACS-4.5.6 simulation package.[45]

■ RESULTS AND DISCUSSION

Contact Angle Calculations. The initially cubic water droplet reshapes into a hemicircular droplet during the course of the simulation, as shown in Figure 2. We consider three different kinds of crystalline surfaces: (111), (110), and (001) facets of FCC, BCC, and HCP structure, respectively, to investigate the effect of crystallographic symmetry on wettability of the material. The contact angle of a droplet is

measured by following a method described in ref 46. Briefly, this approach is a two-step method that first defines a water droplet density profile on the solid surface, and then fits a circle through the top surface of that profile, defined by the locus of positions at which the density drops to half that of bulk water. To carry this out, the xy plane is defined as the plane parallel to the layers of the substrate surface while the z-axis is the axis passing through the center of mass of the droplet normal to the xy plane, with position $z = 0$ defined by the centers of the topmost layer of the solid surface, as marked in Figure 3 by the
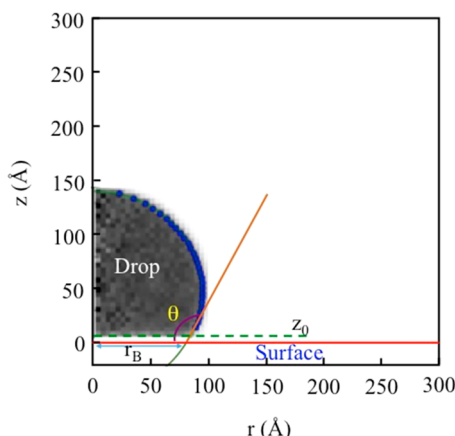

Figure 3. Density profile of the water droplet ($N_w = 9694$).

red horizontal line. The water density profiles are obtained by averaging over an MD simulation trajectory with water bead positions accumulated in cylindrical bins. Since the droplet shape has radial symmetry, we define a point P using (r, z) coordinates, where r is the distance from the center of the droplet in the xy plane. The droplet volume is discretized into rings of height $\Delta z = 0.1$ nm that span from r to $r + dr$, where $dr = 0.1$ nm. The radial location $R(z)$ of the droplet interface against the vacuum for each z-slice is determined as the position at which the density is half of bulk water using the following density relation for the liquid–gas interface

$$\rho(r, z) = \frac{\rho_l}{2}\left(1 - \tanh\left[\frac{2(r - R(z))}{w(z)}\right]\right) \tag{1}$$

where the vapor density is assumed to be zero, ρ_l is the density of bulk liquid, r is the radial distance from the z axis to the droplet surface, $R(z)$ is the center of the interface region, and $w(z)$ is the z-dependent interface thickness. In the second step, the best-fit circle through the boundary points $R(z)$ is extrapolated to the first layer of the substrate surface (at $z = 0$ as defined above), which gives the microscopic contact angle θ as the local slope of the circle at this point of intersection (see Figure 3). Since the centers of mass of the lowest layer of water beads lie slightly above the substrate surface and the water bead center of mass density therefore becomes small within a thin layer just above the substrate surface, we use the water density profile down to a height of $z_0 = 8$ Å (which is marked in Figure 3 by a green horizontal line), and extrapolate the circle the rest of the distance to $z = 0$ where the contact angle is defined.

The macroscopic contact angle θ_∞ is then calculated by fitting a set of microscopic contact angles (θ) for various sized droplets to the modified Young's equation that accounts for droplet size through inclusion of the line tension,[47] as given below.

$$\gamma_{SV} = \gamma_{SL} + \gamma_{LV} \cos\theta + \frac{\tau}{r_B} \tag{2}$$

In the above, the γ's are surface tensions between pairs of materials, namely, solid (S), liquid (L), and vapor (V) phases, while τ is the line tension and r_B is the droplet base radius.

We simulate eight droplets of different sizes for each bead type. The microscopic contact angle for each droplet is measured using the method described above, and the droplet base radius r_B is taken as $r_B = R(0)$ for the z-slice where the extrapolated droplet intersects with the surface plane. Figure 4
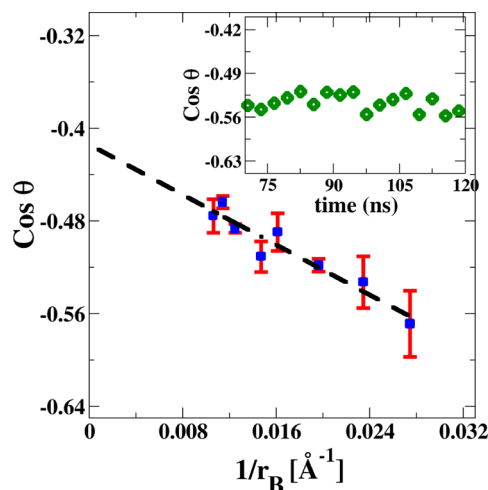

Figure 4. Cosine of the contact angle as a function of the droplet base curvature for the (111) FCC surface composed of beads of type C1. The inset represents the contact angle of the material as a function of the simulation time.

shows $\cos\theta$ as a function of the curvature of the droplet base radius ($1/r_B$) for eight different droplets on a crystalline surface composed of type C1 beads, where "C1" designates a very hydrophobic bead type within the MARTINI force field. For each droplet, the contact angle is calculated for every 3 ns over the last 60 ns of simulation time in order to minimize the error in the calculated contact angle (inset of Figure 4). Then, the averaged contact angle for each droplet is calculated and the macroscopic contact angle is obtained by extrapolating to infinite droplet size (zero value of $1/r_B$) as described in the modified Young's equation (eq 2). This method was implemented earlier in the work of Park and Aluru[48] for atomistic simulations of droplets on substrates such as TiO_2.

However, the MARTINI model has the well-known problem that the water beads in the bulk have a freezing point between 280 and 300 K. This freezing can ordinarily be suppressed by adding 10–12% of "anti-freeze" particles, which are larger in size than regular MARTINI water beads, to the regular water beads. However, when the water molecules are simulated on top of a flat crystalline surface, we find that, to suppress freezing, we need to add 20% antifreezing particles of the total number of water beads (in particular for hydrophilic surfaces) to the regular water beads. We note that these extra antifreeze particles have little effect on the contact angle measurement, as shown by comparing the contact angle obtained with 20% antifreeze with that for 10% antifreeze beads (Table 1). (Although the water beads adjacent to the surface crystallize with 10% of antifreezing beads, the contact angle proves to be little affected by this crystallization.) Therefore, 20% antifreeze

Table 1. Macroscopic Contact Angles from Extrapolation of Microscopic Contact Angles for Eight Droplets of Differing Sizes, as Illustrated in Figure 4[a]

bead type	$\theta_\infty^{FCC}(111)$	$\theta_\infty^{BCC}(110)$	$\theta_\infty^{HCP}(001)$
C1	114.42 ± 0.88 (114.23 + 0.78)	116.02 ± 1.07	113.64 ± 0.61
C2	88.48 ± 0.69 (87.28 + 0.94)	92.4 ± 0.56	83.58 ± 0.84
C3/C4	76.90 ± 0.94 (72.46 + 1.06)	83.79 ± 0.86	74.22 ± 0.83
C5	69.64 ± 0.82 (65.68 + 0.83)	73.34 ± 1.02	63.08 ± 0.76
C6	57.95 ± 0.98	64.23 ± 0.76	52.64 ± 0.86
C7	47.46 ± 0.74	50.36 ± 0.84	43.43 ± 0.79
C8	40.54 ± 0.92	42.23 ± 0.92	36.94 ± 0.96
N0	21.50 ± 1.11		
Na	18.55 ± 0.92		
Nd	18.21 ± 0.89		
Nda	17.26 ± 0.76		

[a]Values correspond to the contact angles with 20% anti-freezing water beads, except for values reported in parentheses, which are for 10% anti-freeze. Note that the contact angles of water for C3 and C4 bead type are the same as the self-interaction and cross-interaction parameters with water are the same for these two bead types.

particles are used in all of the simulations, except for a few test cases with 10% antifreeze particles, and the corresponding extrapolated macroscopic contact angles are reported in Table 1.

As shown in Table 1, for a surface composed of beads of type C1, the interaction between surface and water is the most repulsive, leading to a contact angle of 114°, while, for surfaces with bead types "Nd", "Na", and "Nda", which are much more hydrophilic bead types, the contact angle is much smaller (∼20°). In the case of a polar bead type ("P"), the water−surface attraction is so strong that the droplet completely spreads out on the surface, leading to a zero contact angle for all droplet sizes (results not shown). To test for equilibration, we use the equilibrated droplet on a C5 surface, which has a microscopic contact angle of 69°, as an initial condition, and run the simulations for C1, for a microsystem with a droplet possessing 7640 water beads. Following this change in surface bead type, the new contact angle after re-equilibration increases to 116.40 ± 1.24°, which is close to the value of 119.33 ± 2.15° obtained on this C1 surface when a cubic droplet is used (as described earlier) as the initial configuration for the simulations. This demonstrates that the contact angles calculated from the initially cubic droplet are sufficiently equilibrated to be reliable. We also find that the contact angles of water are slightly higher on BCC surfaces than on FCC or HCP surfaces. However, the differences are not very significant, and we can largely ignore them.

The calculated contact angles for surfaces with different bead types and symmetries, presented in Table 1, range from 114° for C1 bead type to 69° for the C5 bead type of the MARTINI force field, with contact angles of zero for all "P" and "Q" bead types. We note that the value of 114° for C1 is consistent with the experimental contact angle for water on smooth paraffin, which is around 105−110°,[49] which is expected, since the C1 bead type is typically used for alkanes within MARTINI. The surface can then be classified as super hydrophobic ($\theta_\infty > 150°$), hydrophobic ($65° < \theta_\infty < 150°$), hydrophilic ($0° < \theta_\infty < 65°$), or super hydrophilic ($\theta_\infty \approx 0°$).[50,51] Since these conventional MARTINI beads produce no intermediate hydrophilic surfaces (with contact angles between $30° < \theta_\infty < 65°$), we introduce here three new MARTINI bead types by

linearly interpolating between C5 (apolar) and N0 (intermediate polar) bead types, allowing us to make hydrophilic surfaces with relatively smaller contact angles (40−65°). We name the new bead types C6, C7, and C8. As the self-interaction LJ parameters for C5 and N0 are the same, the self-interaction parameters for C6, C7, and C8 are assumed to be the same as well. It is the cross interaction terms between these new bead types and the water bead type (P4) that differ, and these are obtained by interpolating linearly between the cross interaction parameters for C5−P4 and N0−P4. The Lennard-Jones (LJ) parameters for self-interactions and cross interaction with water of the three new bead types are given in the Supporting Information. The cross interaction parameters between these new beads and the rest of the MARTINI bead types used in our simulations can also be found in the Supporting Information. The contact angles of these new bead types, ranging from 40 to 58°, along with those for conventional MARTINI bead types, are given in Table 1. The new bead types allow us to model surfaces with intermediate hydrophilic character. In Figure 5, we show the
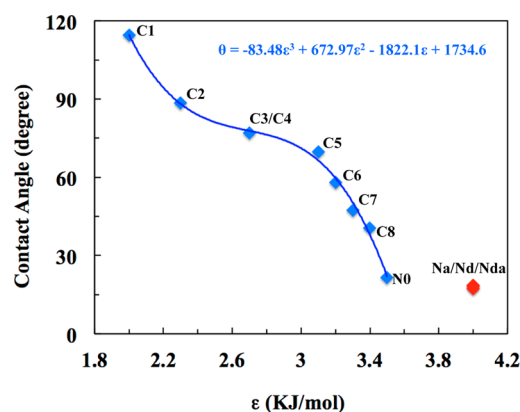

Figure 5. Contact angle as a function of the water−surface interaction strength for the FCC surface. The solid line is a third order polynomial fitting. Contact angles for Na, Nd, and Nda are not included in the fitting.

contact angle as a function of water−surface interaction strength for the FCC surface. There is a sharp drop in the contact angle near $\varepsilon = 3.1$ ($\theta_\infty \approx 65°$), which is the signature of a hydrophobic-to-hydrophilic transition. Later we will show that lipids interact with the NP differently below and above this contact angle.

Now we discuss the reliability of the contact angle values of the MARTINI water obtained from the coarse-grained simulations. It is well-known that the MARTINI model poorly reproduces the water/air surface tension. The experimental surface tension of the water/air interface is 73 mN/m, whereas a value of 30 mN/m is predicted by the MARTINI model.[32] Thus, one would expect the contact angle obtained from the MARTINI model to be inaccurate. However, as we mentioned earlier, the contact angle of MARTINI water on the "C1" FCC surface is 114°, which is close to the experimental contact angle of water on smooth paraffin (105−110°),[49] which is usually modeled using the C1 bead type. To understand this better-than-expected agreement, we use the MARTINI model to calculate the surface tension values of different interfaces of dodecane for which the experimental surface tension values are known. Dodecane is modeled using the C1 bead type, as proposed by Marrink et al.[32] The surface tension values are

Table 2. Surface Tension of Water/Air, Dodecane/Air, and Water/Dodecane Interfaces

interface/model	MARTINI	polarizable MARTINI	BMW-MARTINI	experimental value
water/air (mN/m)	29.6	30.9[a]	77.8	73[32]
	30.0[32]	34.9[b]	77.0[53]	
		30.5[52,a]		
dodecane/air (mN/m)	22.8	22.8	22.8	24[32]
	23.0[32]			
water/dodecane (mN/m)	40.7	51.9	93.3	52[32]
	50.0[32]			

[a]The shift method was used for electrostatic energy computation. [b]The PME method was used for electrostatic energy computation.
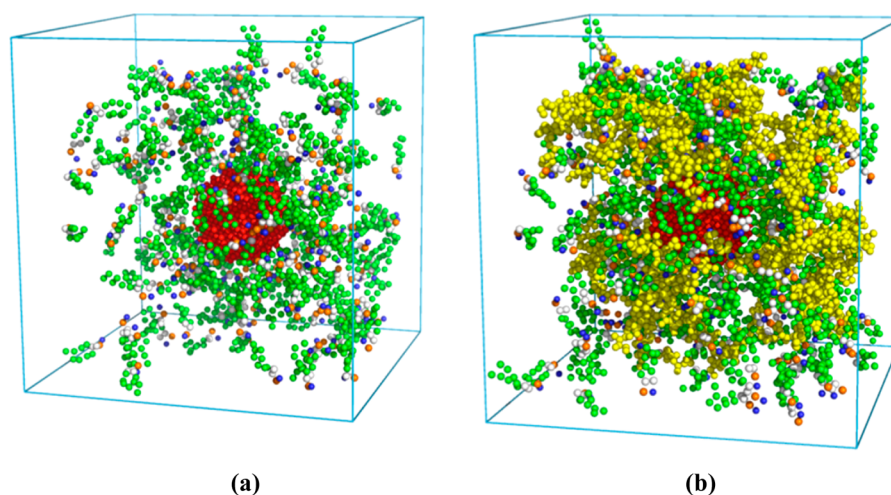
Figure 6. Initial configuration of (a) NP-DPPC and (b) NP-DPPC-SP-C systems. Water is omitted for clarity.

given in Table 2. We refer the reader to the Supporting Information for details of the surface tension calculation. Here we simply note that we obtain a different surface tension value for the dodecane/water interface from what Marrink et al.[32] reported for this interface. Marrink et al. observed a size dependence of this value, which also contradicts our results, as we show in the Supporting Information. The MARTINI model underestimates two of the three interfacial surface tensions, namely, γ_{VL} and γ_{SL}. Using the MARTINI surface tensions, the macroscopic contact angle of water on dodecane from Young's equation is $\theta_\infty = \cos^{-1}[(\gamma_{SV} - \gamma_{SL})/\gamma_{VL}] = \cos^{-1}[(22.8 - 40.7)/29.6 = 127°$, while from the corresponding experimental surface tensions one obtains $\theta_\infty = \cos^{-1}[(24 - 52)/73] = 113°$. The two contact angles are reasonably close, since the poor surface tension value of the water/air interface obtained from the MARTINI model is largely canceled out by a similar error in the water/dodecane surface tension. Note that the contact angle of water on the dodecane surface (modeled by the C1 bead type) is similar to the contact angle value of the water on the C1 FCC surface (114°) that we predicted above.

Recently, two other CG models of water, namely, the polarizable MARTINI water[52] and the BMW model,[53] were proposed as models that reproduce bulk water properties more realistically than the regular MARTINI water model can. To test whether these models might be better models for predicting contact angles, we calculate the interfacial surface tensions they give for dodecane and water and compare them with the experimental values in Table 2. The polarizable MARTINI model reproduces the water/dodecane surface tension correctly, but it still poorly reproduces the water/air interfacial tension. On the other hand, the BMW model correctly reproduces the water/air surface tension but over-

estimates the water/dodecane interfacial tension. From these values, the contact angle of water on the dodecane surface is $\theta_\infty = \cos^{-1}[(22.8 - 51.9)/34.9] = 147°$ and $\theta_\infty = \cos^{-1}[(22.8 - 93.3)/77.8] = 155°$ for the polarizable water and BMW models, respectively. Note that these two values are much higher than the experimental value (113°). This is expected, since only one of the three surface tension values is wrongly estimated in both the polarizable water and the BMW water model and hence the wrongly estimated surface tension value is not canceled out in the contact angle calculations.

To verify further, we calculate the contact angle of BMW water on the FCC crystal surface (Figure S1 of the Supporting Information) and the values are 146.5, 139.4, 126.7, 122.6, and 113.8° for C1, C3, N0, Nda, and P1 bead types, respectively. These are much higher than what is predicted by the MARTNI model. This is expected, as we already mentioned the BMW model overestimates the hydrocarbon/water surface tension. We also put a BMW water droplet on a P4 FCC crystal surface and equilibrate it at 298 K for 140 ns. One would expect the water droplet to spread over the crystal surface, as the "P4" is one of the most polar bead types. However, the BMW water droplet adapted a stable hemicircular shape on the crystal surface, as shown in Figure S2 of the Supporting Information. Thus, we conclude the BMW water is not suitable for modeling the hydrophobicity of the nanoparticles. We also attempt to obtain the contact angle of polarizable water on FCC crystal surfaces of bead types C1 and N0, but the water droplets completely crystallize (Figure S3 of the Supporting Information), as might be expected in the absence of a suitable antifreeze bead for polarizable water. The contact angles obtained may therefore be unreliable, as the droplets may not adapt the correct structure before they are frozen. Their values,
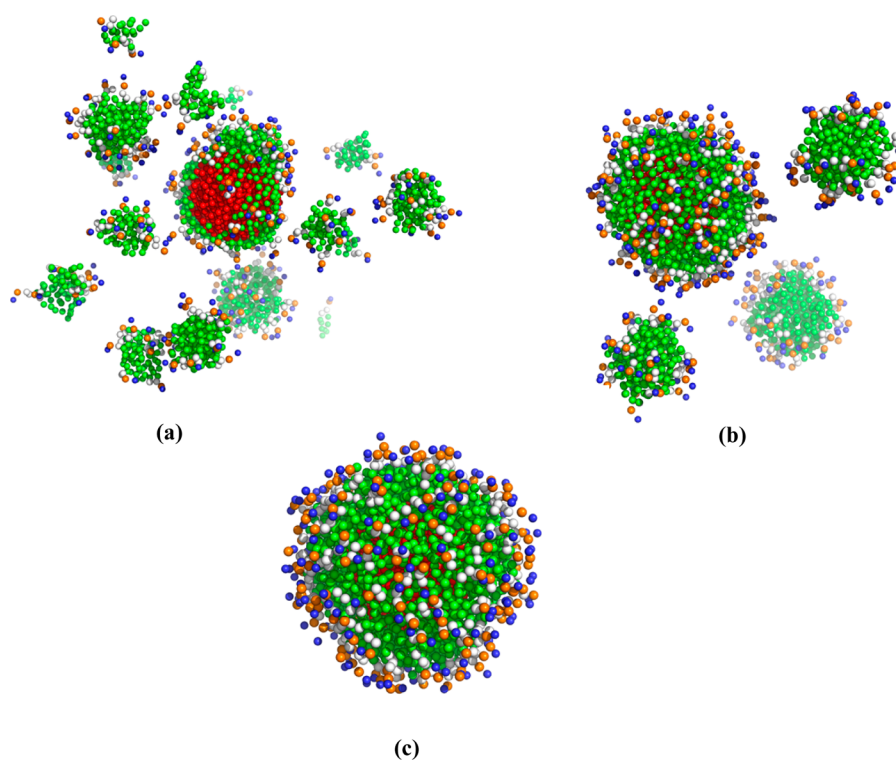
Figure 7. Snapshots of the DPPC corona formation process at (a) 10 ns, (b) 100 ns, and (c) 260 ns around a C1 bead type NP.
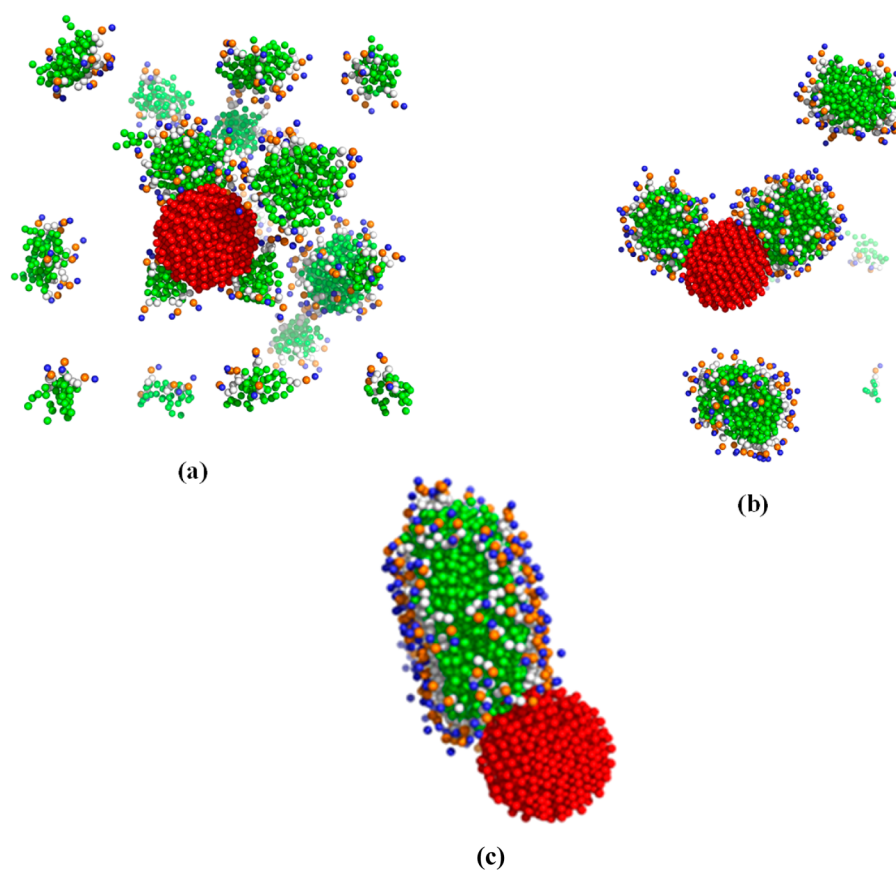

Figure 8. Snapshots of the DPPC corona formation process at (a) 20 ns, (b) 55 ns, and (c) 500 ns around an N0 bead type NP.

given in the Supporting Information, are close to the corresponding MARTINI water values.

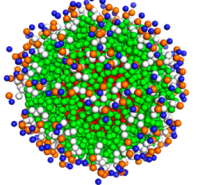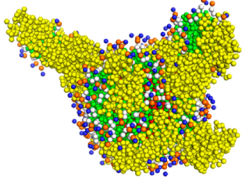Thus, on the basis of our results for the water contact angle on the dodecane surface, the MARTINI model is likely to predict the contact angle of water on a substrate more
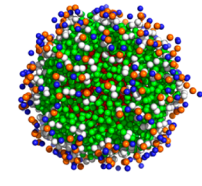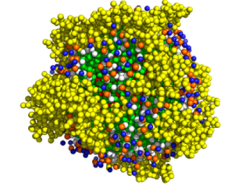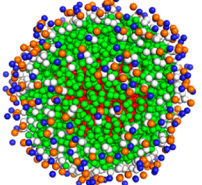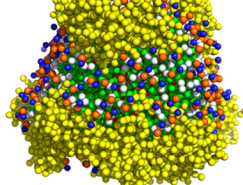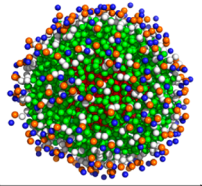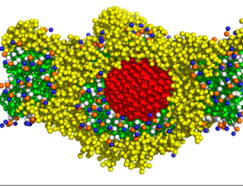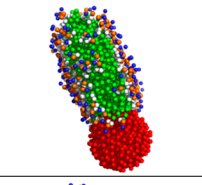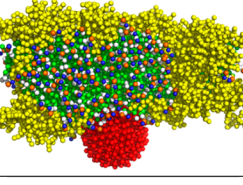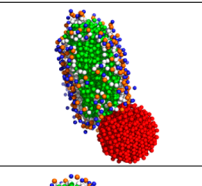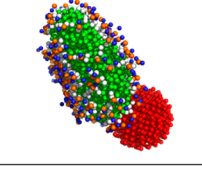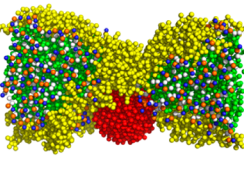
Bead type	Hydrophobicity	Interaction between NP & DPPC	Interaction between NP, DPPC & SP-C peptide
C1	θ = 114.42°		
C2	θ = 88.48°		
C3	θ = 76.90°		
C5	θ = 69.64°		
C7	θ = 47.46 °		
N0	θ = 21.50°		
Nda	θ = 17.26°		

Figure 9. Corona formation around NP as a function of NP surface hydrophobicity.

accurately than the other two models do, especially for hydrophobic substrates. However, the MARTINI model underestimates the water/air and the hydrocarbon/water surface tensions. In the next section, we will discuss the interactions of the NPs of different bead types with the DPPC lipids using the MARTINI, polarizable MARTINI, and BMW water models. We will also show how the lipids interact with the NP for each water model.

Interaction of NPs with Lipids. In this section, we first discuss the interaction of DPPC lipids with nanoparticles (NPs) as a function of NP hydrophobicity using the MARTINI

model. A spherical NP of 5 nm diameter is built from a bulk FCC crystal and put in the center of a 15 nm cubic box. Each bead of the NP is connected to neighboring beads by a harmonic bo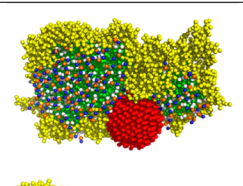nd, to prevent any crystal reconstruction. The NP is allowed to rotate and translate during the course of the simulation. To investigate the interaction of lipids with this NP, 200 DPPC lipids are randomly placed in the simulation box using the "genbox" module of GROMACS, as shown in Figure 6. The simulation box is then solvated with MARTINI water beads. As mentioned before, we use 20% antifreeze particles to block freezing of the MARTINI water. The initial system is

energy minimized, followed by an equilibration for 5 μs at 1.0 bar pressure and 298 K temperature. A V-rescale thermostat[44] and Berendsen barostat[54] are employed to control the temperature and pressure, respectively. A cutoff of 1.2 nm is used for both the van der Waals and electrostatic interactions. We use a time step of 20 fs for the simulations containing lipids. We consider only NPs cut from FCC crystals, since the contact angles for different crystal symmetries are not too different, and in any event change in a systematic way, as shown in Table 1.

In all of the simulations, we observe spontaneous corona or micelle formation of the lipids around the NP during the course of the simulation. Figure 7 and Figure 8 show the representative snapshots of the corona formation process around a hydrophobic NP and a micelle-like structure formation process around a hydrophilic NP, respectively. In the corona/micelle formation process, multiple small micelles are initially formed in the solution. These small micelles aggregate to form bigger micelles in the solution, which are then directly adsorbed on a hydrophobic surface. However, in case of a hydrophilic surface, multiple small micelles are initially adsorbed to the NP surface (Figure 8a,b). These individual NP-attached micelles grow by adsorbing lipids from the solution. When they have grown large enough, the micelles aggregate to form a bigger single micelle attached to the NP surface, as shown in Figure 8c. The final structures obtained for different kinds of NPs after 5 μs long simulations are presented in Figure 9. The DPPC lipids form a corona around the hydrophobic NPs (bead types C1−C5), as the hydrophobic lipid tails are bound to the hydrophobic NP surface while the hydrophilic lipid heads are exposed to the water. The situation changes near the vicinity of hydrophilic surfaces (C6, C7, N0, and Nda), where a micelle-like structure is formed and a small part of the micelle is attached to the NP. This structure appears to be analogous to the binding of rod-like micelles to NP−surfactant complexes described in simulations with the MARTINI force field by Sambasivam et al.[39] The rest of the NP remains exposed to the water. The NP−micelle complex structures are observed for all hydrophobic NPs (C6, C7, N0, and Nda beads) and are stable during the 5 μs long simulation run, confirming the stability of these complex structures. The transition from a tail-coated NP surface to a micelle attached to the NP surface occurs at a contact angle of around 58°, which is within the range of hydrophilic materials ($0° < \theta_\infty < 65°$). We computed the radial distribution function (RDF) between the NP beads and lipid beads to scrutinize the complex structures formed by the lipids and NPs. As expected, the density of lipid tails is large near the hydrophobic surface and decreases near the hydrophilic surface (Figure 10). Interestingly, we observe that the lipid density near the NP surface is very similar for all NPs with a contact angle above approximately 58°. Below this contact angle, the lipid density near the NP surface sharply drops to a low value, suggesting a first-order-like transition of the DPPC lipid density near the NP surface.

Nanoparticles made of FCC material usually adapt a faceted structure containing [100] and [111] surfaces, rather than the more spherical surfaces studied above. Thus, we also investigate the effect of NP shape on interactions of DPPC lipids with an FCC NP containing eight [111] and six [100] surfaces, as shown in Figure S4. We perform the simulations with a C5 NP, the least hydrophobic material for which a corona forms, and with a C7 NP, the most hydrophobic material for which an attached micelle structure forms. As can be seen in Figure S4, the DPPC lipids form a corona around the faceted C5 NP and
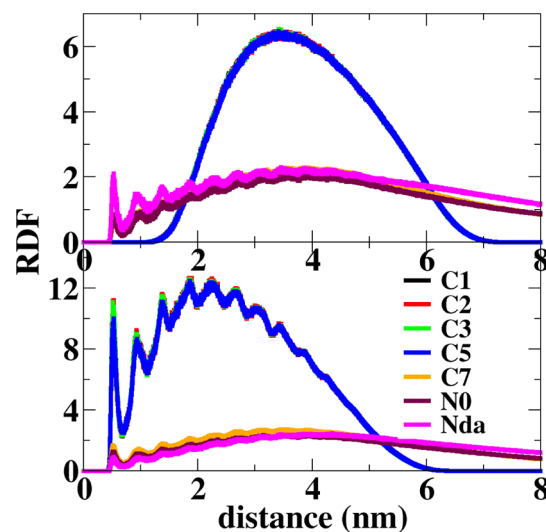

Figure 10. Radial distribution function (RDF) between all the NP beads and DPPC head (upper panel) and tail beads (lower panel). All data for bead types C1−C5 are superposed onto essentially a single line, with the remaining data for C7 through Nda superposed on a second line.

form a micelle structure attached to the C7 NP surface, just as they did for the corresponding spherical NPs. Thus, we conclude the shape of a very small NP has little effect on its interaction with DPPC lipids.

We also carry out simulations of NP−lipid interactions in the presence of BMW and polarizable MARTINI water. We first discuss the results obtained from the BMW model. The cubic simulation box (15 nm) containing a single NP and 200 randomly dispersed DPPC lipids is solvated using the BMW water. The system is energy minimized, heated, and equilibrated in the same way as we described before. In the final structure obtained after a 1 μs long simulation, shown in Figure S5, the lipids form a corona around the NP composed of C5, N0, or Nda beads and form micelles attached to P1 NP. This is expected, since the BMW model overestimates the water/hydrocarbon surface tension and hence the contact angle of water is much higher than that of the MARTINI water for all bead types, as we already described earlier. Thus, each CG bead type is more hydrophobic for the BMW model. As a result, we observe the transition from tails coating the NP surface to a hemimicelle attached to water-wet NPs near a contact angle of 113.8° (P1 bead type) which is much higher than the transition angle of 58° predicted by the MARTINI model. However, it seems unlikely that lipids would form a micelle structure attached to a NP made of a material having a contact angle as much as 113.8°, since this contact angle indicates a hydrophobic material for which lipids should form a corona structure. Thus, we conclude that the BMW model is not suitable for modeling the hydrophobicity of the NPs, while the MARTINI model gives more reasonable predictions.

We now present the results of the NP−lipid interactions in the presence of polarizable MARTINI water. The lipids form a corona for a C5 NP and hemimicelles attached to the NP surface for an N0 NP, as shown in Figure S6, just as observed for these bead types in the MARTINI model. There are some small differences relative to the MARTINI simulations, such as the presence of a small free-floating micelle not part of the corona for the C5 NP and the presence of two, rather than one hemimicelle, attached to the N0 NP, as shown in Figure S6.

(These small differences might disappear if runs longer than 1 μs could be carried out.) The similarity in results for polarizable and MARTINI water suggest that the hydrocarbon/water surface tension is probably more important in determining the lipid−NP interaction rather than the water/air surface tension. The hydrocarbon/water surface tensions for the dodecane/water interface obtained from the MARTINI water (40.7 mN/m) and polarizable MARTINI water (51.9 mN/m) differ but not by much, and hence, these two models predict similar structure in the NP−lipid interactions. However, the BMW model predicts the hydrocarbon/water surface tensions much higher (93.3 mN/m for the dodecane/water compared with the experimental value of 52 mN/m) and hence cannot predict the NP−lipid interactions correctly. However, as we mentioned earlier, the polarizable MARTINI model cannot predict the contact angle correctly and thus we suggest one should use the MARTINI water to model the NP hydrophobicity. The hydrocarbon/water surface tension is about 20% too low for MARTINI water, but for NP−DPPC lipid interactions, this modest discrepancy does not seem to affect the NP−lipid interaction much, as shown by the similar results obtained with the polarizable MARTINI water, which give the correct hydrocarbon/water surface tension. In the next section, we discuss the interaction of NP−lipids in the presence of SP-C peptides.

Interaction of NPs with Lipid and Peptide Complex. We first investigate the interactions of SP-C peptides with the NPs. SP-C is a 31-residue amphipathic peptide found in lung surfactant.[55] The atomic structure of the SP-C peptide and its amino acid sequence are shown in Figure S7. The structure and topology of the coarse-grained peptide are generated using the "martinize.py" script publicly available in the MARTINI webpage.[56] SP-C peptide contains both hydrophobic (proline, alanine, glycine, phenylalanine, isoleucine, valine, and leucine) and hydrophilic (serine, aspartic acid, tyrosine, arginine, histidine, and lysine) residues. Therefore, we consider two NPs: one hydrophobic (C1 bead type) and another hydrophilic (N0 bead type). The SP-C peptides interact in a very similar way with both the hydrophobic and hydrophilic NPs. They do not form any corona structure around a hydrophobic (C1) NP as DPPC lipids do; rather, they form an aggregate that partly covers the NP surface, as shown in Figure S8 for both the hydrophobic and hydrophilic NPs. A large portion of the NP surface is exposed to water. However, part of the NP surface is still covered by the peptides. Thus, the SP-C peptides should compete with the lipids for access to the NP surface in a solution of DPPC and SP-C mixture. We also carry out simulations of a NP/DPPC/SP-C complex to investigate the effect of SP-C peptides on the NP−DPPC interactions. A total of 40 SP-C peptides are randomly placed along with 200 DPPC lipids in a 15 nm cubic box, as shown in Figure 6b. The coarse-grained structure of a DPPC lipid contains 12 MARTINI beads, whereas that of a SP-C peptide contains 72 MARTINI beads. Thus, we chose a 1:5 ratio of peptide molecules to lipid molecules so that both components have roughly comparable numbers of MARTINI beads and roughly comparable mass concentrations. We note that, when the NP is hydrophobic (C1−C3 bead type), DPPC sits on the surface and the SP-C peptide resides on top of the lipid head groups, as shown in Figure 9. As the hydrophobicity of the NP decreases, the peptides move closer to the NP surface, with both the lipids and peptides contacting the C5 bead type surface. Figure 9 shows that the peptides remain far away from the more

hydrophilic C7 bead-type NP surface, as the peptide coats the micelle-like structure formed by the lipids at this hydrophobicity. Note that for a C7 NP the interaction between the peptides and lipids is stronger than that between peptides and the NP. Since the lipids form a micelle-like structure and the peptides sit on the circumference of the micelle, the peptides remain far away from the NP, as shown in Figure 9 (C7 bead type) and Figure 11b. As the hydrophobicity decreases further
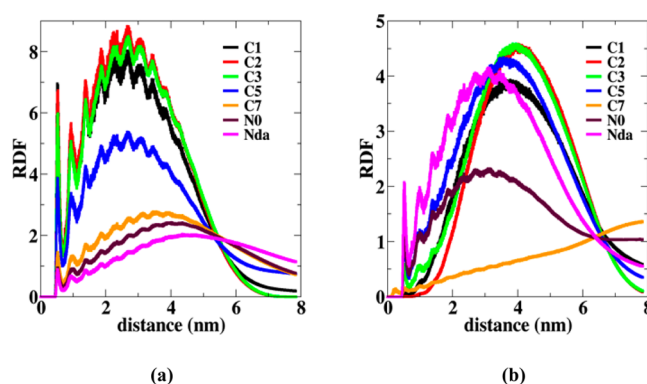

Figure 11. RDF between (a) DPPC beads and (b) SP-C peptide beads with all the NP beads.

(for the N0 bead type), the interaction between the NP and the peptides becomes stronger than that between lipids and peptides, and the density of peptides near the NP surface increases (Figure 11). For an Nda type NP, the peptides are mostly attached to the NP surface while the lipids are pushed away. Thus, a super hydrophilic NP having both donor and acceptor sites has the strongest interaction with the SP-C peptides.

We also investigate the interaction of the NP/DPPC/SP-C complex in the presence of polarizable MARTINI water. We perform the simulations with a C3 NP, the least hydrophobic material for which the peptides reside on top of the lipid corona around the NP, and with a C5 NP, the most hydrophobic material for which the peptides just start to be in contact with the NP surface. As can be seen in Figure S9, the peptides reside on top of the corona structure around the C3 NP and start to be in contact with the C5 NP surface just as they did for the corresponding NPs in the presence of MARTINI water (Figure 9).

■ CONCLUSIONS

We have performed coarse-grained molecular dynamics simulations to model the hydrophobicity of inorganic NPs. We showed that the crystalline surfaces made of different MARTINI beads form a wide range of contact angles with water which allowed us to perform a systematic study of the interaction of NPs with lipid and protein systems as a function of the NP hydrophobicity. We note that the lipids form a corona around a hydrophobic NP whose contact angle with water droplets in a vacuum is higher than ∼60°, but they form a micelle structure attached to the NP surface when the contact angle of the NP is lower than 60°. Interestingly, we observed that the transition from tails coating the NP surface to hemimicelle coating to water-wet NPs as contact angle changes is abrupt, suggesting a first-order-like transition. We also investigated the role of SP-C peptides on the interaction of NP−lipid systems. The NPs with higher hydrophobicity are

covered by the lipids, and the peptides reside on top of the lipid corona. As the hydrophobicity of the NP decreases, the peptides compete with the lipids to access the NP surface. When the hydrophobicity of the NP is close to 20°, most of the NP surface is in contact with the peptides and the lipids sit on top of the peptides. Our calculation of contact angles, and introduction of new bead types, will be helpful in modeling materials in general at the coarse-grained level, by allowing future researchers to choose an appropriate MARTINI bead type whose contact angle with water is similar to that of the material being modeled. For example, Wang et al.[57] experimentally measured the contact angle to be 127 and 98.3° for the graphene and graphite surface, respectively. However, Wu et al.[58] used a C1 MARTINI bead type for both the graphene and graphite surface. Our study suggests that a C1 and C2 type MARTINI bead would be more appropriate for graphene and graphite, respectively.

■ ASSOCIATED CONTENT

⑤ Supporting Information

The Supporting Information is available free of charge on the ACS Publications website at DOI: 10.1021/acs.langmuir.6b01963.

> Tables containing LJ parameters of new beads and surface tension values, interfacial surface tension calculation, and several additional figures (PDF)

■ AUTHOR INFORMATION

Corresponding Author
*E-mail: rlarson@umich.edu.

ORCID ⓘ
Ali Ramazani: 0000-0002-6887-1086

Author Contributions
[†]A.R. and T.M. contributed equally. The manuscript was written through contributions of all authors. All authors have given approval to the final version of the manuscript.

Notes
The authors declare no competing financial interest.

■ ACKNOWLEDGMENTS

■ REFERENCES

(1) You, J.; Chen, C.-C.; Dou, L.; Murase, S.; Duan, H.-S.; Hawks, S. A.; Xu, T.; Son, H. J.; Yu, L.; Li, G.; Yang, Y. Metal Oxide Nanoparticles as an Electron-Transport Layer in High-Performance and Stable Inverted Polymer Solar Cells. *Adv. Mater.* **2012**, *24* (38), 5267−5272.

(2) Fu, L.; Liu, Z. M.; Liu, Y. Q.; Han, B. X.; Hu, P. G.; Cao, L. C.; Zhu, D. B. Beaded cobalt oxide nanoparticles along carbon nanotubes: Towards more highly integrated electronic devices. *Adv. Mater.* **2005**, *17* (2), 217−221.

(3) Ko, S. H.; Pan, H.; Grigoropoulos, C. P.; Luscombe, C. K.; Frechet, J. M. J.; Poulikakos, D. All-inkjet-printed flexible electronics fabrication on a polymer substrate by low-temperature high-resolution selective laser sintering of metal nanoparticles. *Nanotechnology* **2007**, *18* (34), 345202.

(4) Li, Y. N.; Wu, Y. L.; Ong, B. S. Facile synthesis of silver nanoparticles useful for fabrication of high-conductivity elements for printed electronics. *J. Am. Chem. Soc.* **2005**, *127* (10), 3266−3267.

(5) Sridharan, K.; Kuriakose, T.; Philip, R.; Park, T. J. Transition metal (Fe, Co and Ni) oxide nanoparticles grafted graphitic carbon nitrides as efficient optical limiters and recyclable photocatalysts. *Appl. Surf. Sci.* **2014**, *308*, 139−147.

(6) Sathyavathi, R.; Krishna, M. B.; Rao, S. V.; Saritha, R.; Rao, D. N. Biosynthesis of Silver Nanoparticles Using Coriandrum Sativum Leaf Extract and Their Application in Nonlinear Optics. *Adv. Sci. Lett.* **2010**, *3* (2), 138−143.

(7) Khlebtsov, N. G. Optics and biophotonics of nanoparticles with a plasmon resonance. *Quantum Electron.* **2008**, *38* (6), 504−529.

(8) Wang, L.; Clavero, C.; Huba, Z.; Carroll, K. J.; Carpenter, E. E.; Gu, D.; Lukaszew, R. A. Plasmonics and Enhanced Magneto-Optics in Core-Shell Co-Ag Nanoparticles. *Nano Lett.* **2011**, *11* (3), 1237−1240.

(9) Aubry, A.; Lei, D. Y.; Maier, S. A.; Pendry, J. B. Interaction between Plasmonic Nanoparticles Revisited with Transformation Optics. *Phys. Rev. Lett.* **2010**, *105*, 233901.

(10) Mostafalou, S.; Mohammadi, H.; Ramazani, A.; Abdollahi, M. Different biokinetics of nanomedicines linking to their toxicity; an overview. *Daru, J. Pharm. Sci.* **2013**, *21*, 14.

(11) Ling, D.; Hyeon, T. Chemical Design of Biocompatible Iron Oxide Nanoparticles for Medical Applications. *Small* **2013**, *9* (9−10), 1450−1466.

(12) Hamedi-Rad, F.; Ghaffari, T.; Rezaii, F.; Ramazani, A. Effect of nanosilver on thermal and mechanical properties of acrylic base complete dentures. *J. Dent. (Tehran, Islamic Repub. Iran)* **2014**, *11* (5), 495−505.

(13) Hofmann-Amtenbrink, M.; Grainger, D. W.; Hofmann, H. Nanoparticles in medicine: Current challenges facing inorganic nanoparticle toxicity assessments and standardizations. *Nanomedicine* **2015**, *11* (7), 1689−1694.

(14) Lin, W. Introduction: Nanoparticles in Medicine. *Chem. Rev.* **2015**, *115* (19), 10407−10409.

(15) Devadhasan, J. P.; Kim, S. An ultrasensitive method of real time pH monitoring with complementary metal oxide semiconductor image sensor. *Anal. Chim. Acta* **2015**, *858*, 55−59.

(16) Biffi, S.; Voltan, R.; Rampazzo, E.; Prodi, L.; Zauli, G.; Secchiero, P. Applications of nanoparticles in cancer medicine and beyond: optical and multimodal in vivo imaging, tissue targeting and drug delivery. *Expert Opin. Drug Delivery* **2015**, *12* (12), 1837−1849.

(17) Selvan, S. T.; Tan, T. T. Y.; Yi, D. K.; Jana, N. R. Functional and Multifunctional Nanoparticles for Bioimaging and Biosensing. *Langmuir* **2010**, *26* (14), 11631−11641.

(18) Johari-Ahar, M.; Rashidi, M. R.; Barar, J.; Aghaie, M.; Mohammadnejad, D.; Ramazani, A.; Karami, P.; Coukos, G.; Omidi, Y. An ultra-sensitive impedimetric immunosensor for detection of the serum oncomarker CA-125 in ovarian cancer patients. *Nanoscale* **2015**, *7* (8), 3768−3779.

(19) Doria, G.; Conde, J.; Veigas, B.; Giestas, L.; Almeida, C.; Assuncao, M.; Rosa, J.; Baptista, P. V. Noble Metal Nanoparticles for Biosensing Applications. *Sensors* **2012**, *12* (2), 1657−1687.

(20) Rocha-Santos, T. A. P. Sensors and biosensors based on magnetic nanoparticles. *TrAC, Trends Anal. Chem.* **2014**, *62*, 28−36.

(21) Couvreur, P. Nanoparticles in drug delivery: Past, present and future. *Adv. Drug Delivery Rev.* **2013**, *65* (1), 21−23.

(22) Bao, G.; Mitragotri, S.; Tong, S. Multifunctional Nanoparticles for Drug Delivery and Molecular Imaging. *Annu. Rev. Biomed. Eng.* **2013**, *15*, 253−282.

(23) Syamchand, S. S.; Sony, G. Multifunctional hydroxyapatite nanoparticles for drug delivery and multimodal molecular imaging. *Microchim. Acta* **2015**, *182* (9−10), 1567−1589.

(24) Heikkila, E.; Martinez-Seara, H.; Gurtovenko, A. A.; Vattulainen, I.; Akola, J. Atomistic simulations of anionic Au-144(SR)(60) nanoparticles interacting with asymmetric model lipid membranes. *Biochim. Biophys. Acta, Biomembr.* **2014**, *1838* (11), 2852−2860.

(25) Fortunelli, A.; Monti, S. Simulations of lipid adsorption on TiO2 surfaces in solution. *Langmuir* **2008**, *24* (18), 10145−10154.

(26) Vacha, R.; Martinez-Veracoechea, F. J.; Frenkel, D. Receptor-Mediated Endocytosis of Nanoparticles of Various Shapes. *Nano Lett.* **2011**, *11* (12), 5391−5395.

(27) Prates Ramalho, J. P.; Gkeka, P.; Sarkisov, L. Structure and Phase Transformations of DPPC Lipid Bilayers in the Presence of Nanoparticles: Insights from Coarse-Grained Molecular Dynamics Simulations. *Langmuir* **2011**, *27* (7), 3723−3730.

(28) da Rocha, E. L.; Caramori, G. F.; Rambo, C. R. Nanoparticle translocation through a lipid bilayer tuned by surface chemistry. *Phys. Chem. Chem. Phys.* **2013**, *15* (7), 2282−2290.

(29) Nangia, S.; Sureshkumar, R. Effects of Nanoparticle Charge and Shape Anisotropy on Translocation through Cell Membranes. *Langmuir* **2012**, *28* (51), 17666−17671.

(30) Hu, G.; Jiao, B.; Shi, X.; Valle, R. P.; Fan, Q.; Zuo, Y. Y. Physicochemical Properties of Nanoparticles Regulate Translocation across Pulmonary Surfactant Monolayer and Formation of Lipoprotein Corona. *ACS Nano* **2013**, *7* (12), 10525−10533.

(31) Simonelli, F.; Bochicchio, D.; Ferrando, R.; Rossi, G. Monolayer-Protected Anionic Au Nanoparticles Walk into Lipid Membranes Step by Step. *J. Phys. Chem. Lett.* **2015**, *6* (16), 3175−3179.

(32) Marrink, S. J.; Risselada, H. J.; Yefimov, S.; Tieleman, D. P.; de Vries, A. H. The MARTINI force field: Coarse grained model for biomolecular simulations. *J. Phys. Chem. B* **2007**, *111* (27), 7812−7824.

(33) Sangwai, A. V.; Sureshkumar, R. Coarse-Grained Molecular Dynamics Simulations of the Sphere to Rod Transition in Surfactant Micelles. *Langmuir* **2011**, *27* (11), 6628−6638.

(34) Nawaz, S.; Carbone, P. Coarse-Graining Poly(ethylene oxide)-Poly(propylene oxide)-Poly(ethylene oxide) (PEO-PPO-PEO) Block Copolymers Using the MARTINI Force Field. *J. Phys. Chem. B* **2014**, *118* (6), 1648−1659.

(35) Rossi, G.; Monticelli, L.; Puisto, S. R.; Vattulainen, I.; Ala-Nissila, T. Coarse-graining polymers with the MARTINI force-field: polystyrene as a benchmark case. *Soft Matter* **2011**, *7* (2), 698−708.

(36) Uusitalo, J. J.; Ingolfsson, H. I.; Akhshi, P.; Tieleman, D. P.; Marrink, S. J. Martini Coarse-Grained Force Field: Extension to DNA. *J. Chem. Theory Comput.* **2015**, *11* (8), 3932−3945.

(37) Wohlert, J.; Berglund, L. A. A Coarse-Grained Model for Molecular Dynamics Simulations of Native Cellulose. *J. Chem. Theory Comput.* **2011**, *7* (3), 753−760.

(38) Lin, X.; Bai, T.; Zuo, Y. Y.; Gu, N. Promote potential applications of nanoparticles as respiratory drug carrier: insights from molecular dynamics simulations. *Nanoscale* **2014**, *6* (5), 2759−2767.

(39) Sambasivam, A.; Sangwai, A. V.; Sureshkumar, R. Self-Assembly of Nanoparticle-Surfactant Complexes with Rodlike Micelles: A Molecular Dynamics Study. *Langmuir* **2016**, *32* (5), 1214−9.

(40) Tsuda, A.; Konduru, N. V. The role of natural processes and surface energy of inhaled engineered nanoparticles on aggregation and corona formation. *Nanoimpact* **2016**, *2*, 38−44.

(41) Sergi, D.; Scocchi, G.; Ortona, A. Coarse-graining MARTINI model for molecular-dynamics simulations of the wetting properties of graphitic surfaces with non-ionic, long-chain, and T-shaped surfactants. *J. Chem. Phys.* **2012**, *137* (9), 094904.

(42) Yu, G.; Liu, J.; Zhou, J. Mesoscopic coarse-grained simulations of hydrophobic charge induction chromatography (HCIC) for protein purification. *AIChE J.* **2015**, *61* (6), 2035−2047.

(43) Yu, G.; Liu, J.; Zhou, J. Mesoscopic Coarse-Grained Simulations of Lysozyme Adsorption. *J. Phys. Chem. B* **2014**, *118* (17), 4451−4460.

(44) Bussi, G.; Donadio, D.; Parrinello, M. Canonical sampling through velocity rescaling. *J. Chem. Phys.* **2007**, *126* (1), 014101.

(45) Pronk, S.; Pall, S.; Schulz, R.; Larsson, P.; Bjelkmar, P.; Apostolov, R.; Shirts, M. R.; Smith, J. C.; Kasson, P. M.; van der Spoel, D.; Hess, B.; Lindahl, E. GROMACS 4.5: a high-throughput and highly parallel open source molecular simulation toolkit. *Bioinformatics* **2013**, *29* (7), 845−854.

(46) Werder, T.; Walther, J. H.; Jaffe, R. L.; Halicioglu, T.; Koumoutsakos, P. On the water-carbon interaction for use in molecular dynamics simulations of graphite and carbon nanotubes. *J. Phys. Chem. B* **2003**, *107* (6), 1345−1352.

(47) Wang, J. Y.; Betelu, S.; Law, B. M. Line tension approaching a first-order wetting transition: Experimental results from contact angle measurements. *Phys. Rev. E: Stat. Phys., Plasmas, Fluids, Relat. Interdiscip. Top.* **2001**, *63*, 031601.

(48) Park, J. H.; Aluru, N. R. Temperature-dependent wettability on a titanium dioxide surface. *Mol. Simul.* **2009**, *35* (1−2), 31−37.

(49) ZISMAN, W. A. Relation of the Equilibrium Contact Angle to Liquid and Solid Constitution. *Adv. Chem. Ser.* **1964**, *43*, 1−51.

(50) Vogler, E. A. Structure and reactivity of water at biomaterial surfaces. *Adv. Colloid Interface Sci.* **1998**, *74*, 69−117.

(51) Nakajima, A.; Fujishima, A.; Hashimoto, K.; Watanabe, T. Preparation of transparent superhydrophobic boehmite and silica films by sublimation of aluminum acetylacetonate. *Adv. Mater.* **1999**, *11* (16), 1365−1368.

(52) Yesylevskyy, S. O.; Schafer, L. V.; Sengupta, D.; Marrink, S. J. Polarizable Water Model for the Coarse-Grained MARTINI Force Field. *PLoS Comput. Biol.* **2010**, *6* (6), e1000810.

(53) Wu, Z.; Cui, Q.; Yethiraj, A. A New Coarse-Grained Model for Water: The Importance of Electrostatic Interactions. *J. Phys. Chem. B* **2010**, *114* (32), 10524−10529.

(54) Berendsen, H. J. C.; Postma, J. P. M.; Vangunsteren, W. F.; Dinola, A.; Haak, J. R. MOLECULAR-DYNAMICS WITH COUPLING TO AN EXTERNAL BATH. *J. Chem. Phys.* **1984**, *81* (8), 3684−3690.

(55) Walther, F. J.; Waring, A. J.; Hernandez-Juviel, J. M.; Ruchala, P.; Wang, Z.; Notter, R. H.; Gordon, L. M. Surfactant protein C peptides with salt-bridges ("ion-locks") promote high surfactant activities by mimicking the alpha-helix and membrane topography of the native protein. *PeerJ* **2014**, *2*, e485.

(56) http://www.cgmartini.nl/.

(57) Wang, S.; Zhang, Y.; Abidi, N.; Cabrales, L. Wettability and Surface Free Energy of Graphene Films. *Langmuir* **2009**, *25* (18), 11078−11081.

(58) Wu, D.; Yang, X. Coarse-Grained Molecular Simulation of Self-Assembly for Nonionic Surfactants on Graphene Nanostructures. *J. Phys. Chem. B* **2012**, *116* (39), 12048−12056.